3D Angle-of-Arrival Estimation with Practical Antenna Configurations

Shang-Ling Shih, Chao-Kai Wen, *Senior Member, IEEE*, Shi Jin, *Senior Member, IEEE*,
and Kai-Kit Wong, *Fellow, IEEE*

Abstract—With the advances in Internet of Things (IoT) and mobile connectivity, location-based services (LBSs) are increasingly popular and continue to enhance our experience. Multiple antennas have been pivotal for the provision of reliable wireless communications and high-resolution localization. However, in the real world, mobile handsets tend to have very limited space and the incorporation of multiple antennas hardly obeys the rule of half-wavelength separation between antenna elements, resulting in complex mutual coupling. More often than not, antennas are placed not to affect negatively the artistic design and handling of the device. The irregular 3D radiation pattern of each antenna element further impairs the capability of the antenna array for localization. In this paper, we propose a generic parametric model that can incorporate the actual antenna responses into the angle-of-arrival (AoA) estimation. As a result, we present an efficient algorithm to enable 3D AoA estimation on mobile phones based on the proposed model, and test it on a 5G phone at a midband spectrum with $100\mathrm{MHz}$ channel bandwidth. Our results reveal promising performance with over 90% scenarios where the AoA estimation errors are lower than $10°$ on a mobile phone.

Index Terms—5G new radio, angle-of-arrival estimation, channel state information, indoor localization, mobile device.

I. INTRODUCTION

The increasing popularity of mobile devices, coupled with the rise of the Internet of Things (IoT), has resulted in the prevalence of location-based service (LBS) applications, e.g., emergency calls, navigation, object tracking, marketing, and a range of information services [1–3]. Global positioning system (GPS) is currently the *de facto* positioning technology, with approximately $10\mathrm{m}$ accuracy in outdoor environments but its performance in indoor environments is severely degraded due to the lack of line-of-sight (LoS) of the satellites.

For most LBSs, the required indoor positioning accuracy is typically less than $3\mathrm{m}$, which is unfortunately very difficult to achieve by GPS. To overcome this problem, researchers have investigated many indoor positioning systems (IPSs) in recent years [1–13]. The considered media for IPSs include RF-based signals (e.g., 5G, Wi-Fi, Bluetooth, ZigBee, and LPWAN) [1, 2, 4] and non-RF-based signals (e.g., Li-Fi, optical camera communication, and light detection and ranging) [14, 15].

S.-L. Shih and C.-K. Wen are with the Institute of Communications Engineering, National Sun Yat-sen University, Kaohsiung 80424, Taiwan, Email: monlylonly@gmail.com, chaokai.wen@mail.nsysu.edu.tw.

S. Jin is with the National Mobile Communications Research Laboratory, Southeast University, Nanjing 210096, P. R. China, Email: jinshi@seu.edu.cn.

K.-K. Wong is with Department of Electronic and Electrical Engineering, University College London, UK, Email: kai-kit.wong@ucl.ac.uk.

A. Related Work

RF-based positioning is achieved by extracting the location-bearing parameters from the received radio signals. One way is to intersect the time-of-arrival (ToA) or time-difference-of-arrival (TDoA) to find the location of, say a user equipment (UE), through three or more base stations (BSs). Such timing-based positioning technologies usually rely on the support of standards and are radio access technology-dependent (RAT-dependent). For example, 802.11az standardizes a fine timing measurement protocol [16] that enables a pair of devices to estimate their round trip time (RTT). The 3rd Generation Partnership Project (3GPP) New Radio (NR) supports observed TDoA in Release 15 [17] and multi-cell RTT in Release 16 [18]. However, IEEE802.11az is not yet widely used in commercial UE. In addition, the TDoA technique relies on tight synchronization among BSs, whereas the BS synchronization techniques applied by GPSs have clock synchronization errors, causing $30 - 50\mathrm{m}$ errors in positioning [19].

Another common approach bases positioning on angle-of-arrival (AoA) or angle-of-departure (AoD) estimation. Combining direction information using a triangulation process can provide a location estimate without the need of synchronization. The 3GPP NR supports the downlink AoD (DL-AoD) and uplink AoA (UL-AoA) in Release 16 [18]. For DL-AoD, the BS transmits a set of reference signals with beam sweeping. The UE of interest then measures the received signal quality of each beam and reports the measurements to the BSs. On the other hand, for UL-AoA, the BS performs AoA estimations based on the uplink sounding signals sent by the UE. These processes are conducted through the location management function at the core network, and thus are RAT-dependent.

In NR or Wi-Fi, multiple antennas are employed on mobile phones to support enhanced mobile broadband. As such, AoA information can also be available at the UE side without being RAT-dependent. On the one hand, the AoA information can assist the positioning process by combining the information from the RAT-dependent schemes. On the other hand, performing localization from the UE side preserves privacy. Nevertheless, UE tends to have only a limited number of antennas due to their precious space, making it hard to derive precise AoAs. Several AoA estimation techniques based on Wi-Fi and 5G NR have therefore been introduced recently in [20–33].

In particular, ArrayTrack in [20] uses a custom-made WiFi access point (AP) consisting of eight antenna elements and applies MUSIC and spatial smoothing techniques to estimate the AoAs of direct and reflected paths from the UE. Then in
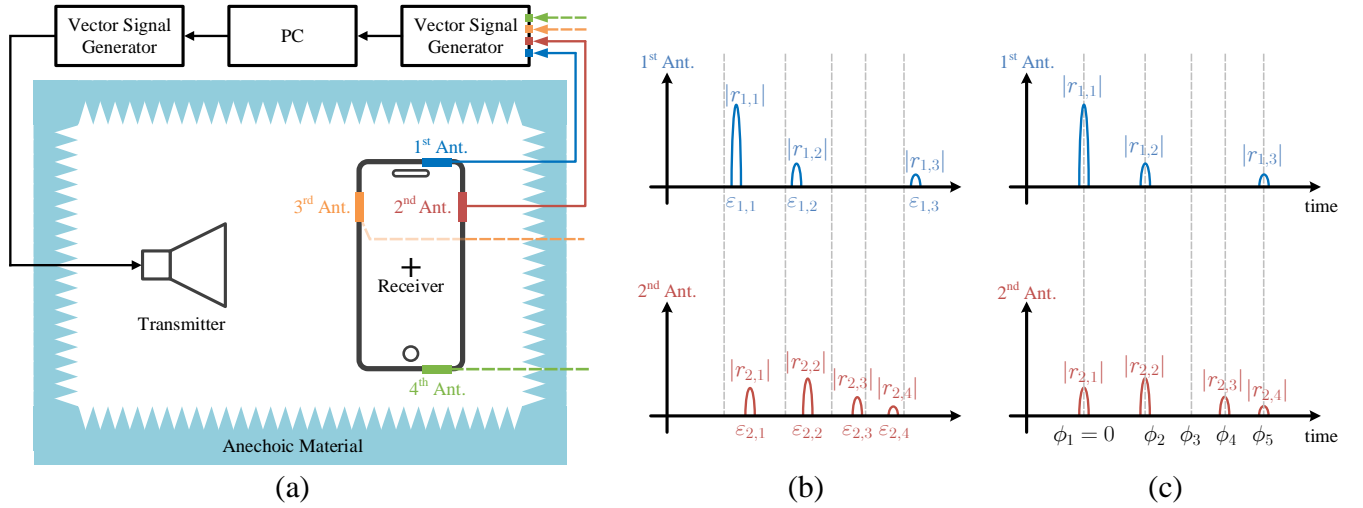
Fig. 1: (a) Measurement setup for antenna response in the anechoic chamber. (b) Original responses. The x-axis is the amplitude of the response, whereas the y-axis is the time difference between ToA and the responses. (c) Aligning the time difference of the responses.

[21], SpotFi employs a typical Wi-Fi AP with three antenna elements and applies MUSIC with a modified spatial smoothing technique to obtain the AoAs and ToAs of the UE. More recently in [22], RoArray which used commercial WiFi AP like SpotFi was also proposed to estimate the AoA and ToA using sparsity-based regularized minimization. It was shown that RoArray outperformed SpotFi at medium or high signal-to-noise ratios (SNRs). Moreover, most recently, [28] proposed MonoLoco to use direct path and multipath reflection from the UE to a single AP for multipath triangulation. BiLoc [29] and SR-PLoc [30] suggested the use of a specific distributed AP for applications with a single-antenna UE to estimate additional ToAs instead of the AoD of the UE for localization.

For 5G NR, [32] proposed to estimate the AoAs with an adjacent angle power difference method based on orthogonal matching pursuit (OMP). Compared with MUSIC, the approach in [32] improved the estimation accuracy and stability. Finally, [33] estimated AoAs for the user-centric ultra-dense network architecture based on an edge cloud.

B. Motivation and Contributions

Despite the progress made so far, it is important to note that in most of the studies, the antennas are tailored specifically for the purpose of positioning, which unfortunately does not reflect the reality when the localization method is used in the real world. In particular, a regular antenna array with spacing of half a wavelength between elements is often assumed. This is however hardly the case in practice due to the limited space at UE. While the antennas on a mobile phone are configured to have low correlation and high isolation, the spacing between the antennas is usually irregular and is not an integer multiple of half a wavelength. Besides, the antennas are connected to a ground plane which makes the response of each antenna highly complex. It is not known how these practical complications can be incorporated into the AoA estimation.

Specifically, our aim is to answer the following questions:

What are the technical challenges brought by practical antennas, and how can 3D AoA estimation be achieved on commodity devices indoors?

To answer these questions, we consider a practical mobile phone system with four antennas and analyze the antenna responses through the over-the-air measurement in the anechoic chamber, as illustrated in Figure 1(a). We then tailor a super-resolution AoA extraction algorithm in the anechoic chamber to analyze the antenna responses. Figure 1(b) shows a single-path producing multiple responses, and that the gain and the number of the responses vary at different antennas and angles. This effect is attributed to the fact that the antennas are close and connected to a ground plane; thus, mutual coupling occurs. The estimation of ToAs and AoAs faces not only the multipath effect resulting from the propagation environment but also the antenna itself. We overcome these challenges by developing a super-resolution AoA estimation algorithm taking into account of the actual antenna responses, implement it on a commodity device and demonstrate the performance using experiments.

In summary, our main contributions are as follows:

- *Generic model for practical antennas*. We study the antenna response and present a novel parameterized model that can integrate the multipath effects resulting from the propagation environment and the antenna responses. The model is universal and includes the conventional ideal antenna as a special case. The model can easily decouple the two multipath sources and therefore, we can use it to develop efficient ToA and AoA estimation algorithms.

- *Efficient algorithm for AoA estimation*. We devise a two-stage algorithm that allows efficient 3D AoA estimation on commodity devices. In the offline stage, we measure the antenna responses at every angle in the anechoic chamber and parameterize them into a 3D table based on the proposed antenna model. In particular, we tailor a
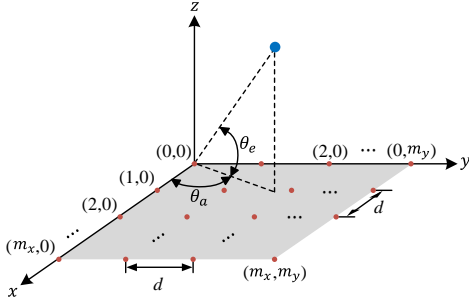
Fig. 2: URA spatial signal model.

super-resolution AoA extraction algorithm for this offline stage. In the online stage, we use this table to synthesize the steering vector for the phone antennas and then apply the synthesized steering vector to identify the AoA of the strongest path from the measured multipath channel. We then remove the identified path and its corresponding antenna responses from the measurement. This procedure is repeated until all the multipaths are extracted. The algorithm can systematically separate all the multipaths and jointly estimate multi-dimensional channel parameters, such as AoAs and ToAs of the multipaths.

- *Implementation on 5G NR.* We implement the algorithm on a 5G NR mobile phone at 3.9GHz band with 100MHz channel bandwidth. We evaluate the effectiveness of the algorithm in indoor environments extensively using both experiments and ray tracing-based computer simulations. Our results suggest that though practical phone antennas lead to complex antenna responses, the phenomenon also diversifies the angular pattern, thereby reducing angular ambiguity. Consequently, the antenna effect is not always a disadvantage but can be desirable to AoA estimation.

The rest of this paper is organized as follows. In Section II, we describe the antenna responses on a mobile phone and introduce our parameterized model for the antenna responses. Section III introduces the proposed estimation algorithm. The measurement and simulation results are shown in Section IV. Finally, in Section V, we provide our concluding remarks.

II. SYSTEM AND ANTENNA MODEL

We consider the transmission system using orthogonal frequency-division multiplexing (OFDM), where the transmission band comprises N subcarriers. The transmitter (Tx) is equipped with a single antenna, and the receiver (Rx) is equipped with M antennas. When the signal propagates through a multipath channel, the channel frequency response (CFR) at the n-th subcarrier of the m-th antenna can be modeled as

$$h_{n,m} = \sum_{l=1}^{L} g_l e^{-j2\pi(n-1)\Delta f \tau_l} a_m(\theta_l), \quad (1)$$

where L is the number of the propagation paths, g_l is the complex gain of the l-th path, Δf is the subcarrier spacing, τ_l is the ToA of the l-th path, θ_l is the AoA of the l-th path, and $a_m(\cdot)$ is the antenna response of the m-th antenna. We have

normalized the antenna response of the first antenna to be 1 and absorbed the phase response into the complex gain g_l.

If Rx is equipped with a uniform rectangular array (URA) (Figure 2), then the antenna response of the m-th antenna of the AoA with the incident path at azimuth angle θ_{a} and elevation angle θ_{e} can be represented as [34]

$$a_{\mathrm{URA},m}(\theta_{\mathrm{a}},\theta_{\mathrm{e}}) = e^{-j2\pi\left(\frac{m_x d}{\lambda}\sin\theta_{\mathrm{a}}\cos\theta_{\mathrm{e}} + \frac{m_y d}{\lambda}\cos\theta_{\mathrm{a}}\cos\theta_{\mathrm{e}}\right)}, \quad (2)$$

where $d = \lambda/2$ is the minimum spacing between two adjacent antennas along the x- or y-axes, m_x and m_y are the integer multiples of the spacing along the x-axis and y-axis of the m-th antenna, and λ is the wavelength of the signal. For the URA, the antenna response reflects the phase differences between antenna elements. However, equipping a URA on a compact phone is difficult. The antennas are usually designed with a particular distribution to be installed on a small-volume phone device and to have low correlation and high isolation. In this case, the spacing between two adjacent antennas is different, and m_x and m_y might not be integer values.

In addition to the irregular antenna spacing, the practical phone antenna brings other issues. To better understand the effects due to a practical phone antenna, we show an experimental result. In the experiment, Rx is equipped with four antennas, and Tx is equipped with a horn antenna as illustrated in Figure 1(a). Given that the measurement is conducted around microwave absorbers to provide a non-reflecting environment, the phone antennas can only receive the line-of-sight (LoS) signal without multipath. We show the responses of every antenna at an angle of incidence. For ease of notation, we use $\theta = (\theta_{\mathrm{a}}, \theta_{\mathrm{e}})$ to denote the angle of incidence. In Figure 1(b), we can observe that the location of the antennas causes different delays to their first response, and the received signal power is also different. In addition to the first impulse response, we find other responses that are elicited from the design of the antennas or the mutual coupling effect. The antenna responses will change in different angles of incidence. These effects are not a concern when using an ideal antenna.

To reflect the effects due to phone antennas, the antenna response of the m-th antenna is modeled as

$$a_{\mathrm{PRA},m}(\theta) = \sum_{j=1}^{J_m(\theta)} |r_{m,j}(\theta)| e^{-j2\pi(n-1)\Delta f \varepsilon_{m,j}(\theta)}, \quad (3)$$

where $J_m(\theta)$ is the number of the response, $|r_{m,j}(\theta)|$ represents the amplitude of the j-th response, and $\varepsilon_{m,j}(\theta)$ is the time difference between ToA and the j-th responses. Notably, these parameters are functions of θ, which implies that these parameters will vary in different angles of incidence. The expression of (3) is general and can include (2) as a special case. For example, in the case of using an ideal URA, the received signal causes only one response for every antenna. Given that $J_m(\theta) = 1$ for every m, $r_{m,j}(\theta)$ and $\varepsilon_{m,j}(\theta)$ in (3) can be simplified as $r_m(\theta)$ and $\varepsilon_m(\theta)$. In addition, the received signal power is equal to every antenna, so we obtain that $|r_m(\theta)| = 1$ for every m. The time difference $\varepsilon_m(\theta)$ is

only caused by the location of the URA and can be written as

$$\varepsilon_m(\theta) = \frac{m_x d \sin\theta_{\mathrm{a}}\cos\theta_{\mathrm{e}} + m_y d \cos\theta_{\mathrm{a}}\cos\theta_{\mathrm{e}}}{(n-1)\Delta f \lambda}. \quad (4)$$

Substituting the above conditions, (3) reduces to (2).

For ease of modeling, we assume the number of the responses is J for every antenna and every angle, which can be determined by selecting the maximum values of $J_m(\theta)$ $\forall m, \theta$. Moreover, we align the sampling points of the antenna responses among antennas. In particular, as in Figure 1(c), we let $\varepsilon_{m,j}(\theta) = \varepsilon'_{m,j}(\theta) + \phi_j(\theta)$, and rewrite (3) as

$$a_{\mathrm{PRA},m}(\theta) = \sum_{j=1}^{J} r_{m,j}(\theta) e^{-j2\pi(n-1)\Delta f \phi_j(\theta)}, \quad (5)$$

where $r_{m,j}(\theta) = |r_{m,j}(\theta)| e^{-j2\pi(n-1)\Delta f \varepsilon'_{m,j}(\theta)}$ has included the amplitude and phase differences among antennas. The antenna response (5) can be regarded as a time-invariant system, which introduces additional multipath at Rx. Combining the channel and the additive noise, the received signal at the n-th subcarrier of the m-th antenna can be expressed as

$$y_{n,m} = h_{n,m} + z_{n,m}, \quad (6)$$

where $h_{n,m}$ is defined by (1) with the *parameterized* antenna response $a_{\mathrm{PRA},m}(\theta)$ given in (5), and $z_{n,m}$ is the additive white Gaussian noise (AWGN).

III. AoA Estimation

Our goal is to estimate the channel parameters (gains, ToAs, AoAs) from cluttering multipaths through measurement $y_{n,m}$. Clearly, the antenna response introducing additional multipaths makes this task more challenging. However, notably, the antenna responses, namely, $r_{m,j}(\theta)$ and $\phi_j(\theta)$ in (5), are not environmental invariant. Thus, they can be determined through an offline measurement in a chamber. The ToA and AoA estimation from the channel with phone antenna is carried out in two stages: offline and online. In the offline stage, the antenna responses at every angle are measured and gathered into a lookup table. In the online stage, we use this table to synthesize a steering vector and then estimate ToAs and AoAs. Both stages apply the Newtonized OMP (NOMP) [35] principle to extract the relevant parameters.

A. Offline Stage: Antenna Response Measurement

In the offline stage, our target is to measure the antenna response at every angle, namely, gathering the parameters of (5). Given that no multipath occurs in the chamber, we set $L = 1$ and simplify $g = g_1$, $\tau = \tau_1$, and $\theta = \theta_1$ in (1), leading to

$$h_{n,m} = \sum_{j=1}^{J} p_{m,j}(\theta) e^{-j2\pi(n-1)\Delta f \delta_j(\theta)}, \quad (7)$$

where

$$p_{m,j}(\theta) = g \cdot r_{m,j}(\theta), \quad \delta_j(\theta) = \tau + \phi_j(\theta). \quad (8)$$

To extract the antenna responses, we keep the distance between Tx and Rx the same at every angle of incidence, so g and τ are unchanged during the measurement. Given that g and τ are angular independent, their values do not affect the ToAs and AoAs estimates in the online stage. Therefore, after estimating $p_{m,j}(\theta)$ and $\delta_j(\theta)$, we can obtain $r_{m,j}(\theta)$ and $\phi_j(\theta)$ by simple normalization and alignment to eliminate g and τ, respectively.

The way to estimate $p_{m,j}(\theta)$ and $\delta_j(\theta)$ is detailed. Given that the estimation is performed for every angle of incidence, we remove the argument θ from $p_{m,j}(\theta)$ and $\delta_j(\theta)$ to make notation concise. From (7), we stack the received signals of N subcarriers of the m-th antenna and express them as a vector form

$$\mathbf{y}_m = \sum_{j=1}^{J} p_{m,j} \mathbf{s}(\delta_j) + \mathbf{z}_m, \quad (9)$$

where

$$\mathbf{s}(\delta) = \left[1, e^{-j2\pi\Delta f \delta}, \dots, e^{-j2\pi(N-1)\Delta f \delta} \right]^{\mathrm{T}}. \quad (10)$$

Particularly, our goal is to estimate

$$\boldsymbol{\delta} = [\delta_1, \delta_2, \dots, \delta_J] \quad (11)$$

and

$$\mathbf{P} = \begin{bmatrix} p_{1,1} & p_{2,1} & \cdots & p_{M,1} \\ p_{1,2} & p_{2,2} & \cdots & p_{M,2} \\ \vdots & \vdots & \ddots & \vdots \\ p_{1,J} & p_{2,J} & \cdots & p_{M,J} \end{bmatrix}. \quad (12)$$

Toward this end, we use the maximum likelihood (ML) estimate

$$(\hat{\mathbf{P}}, \hat{\boldsymbol{\delta}}) = \underset{\mathbf{P}, \boldsymbol{\delta}}{\arg\min} \sum_{m=1}^{M} \left\| \mathbf{y}_m - \sum_{j=1}^{J} p_{m,j} \mathbf{s}(\delta_j) \right\|^2. \quad (13)$$

Given the difficulty of estimating the parameters of J responses simultaneously, we first consider the estimation for a single response, then expand the calculation to all the responses. The ML estimate for one response can be written by

$$(\hat{\mathbf{p}}, \hat{\delta}) = \underset{\mathbf{p}, \delta}{\arg\min} \sum_{m=1}^{M} \| \mathbf{y}_m - p_m \mathbf{s}(\delta) \|^2, \quad (14)$$

where $\mathbf{p}$ is the first row of (12), and we have removed index 1 from $p_{m,1}$. The solution of (14) can be obtained when maximizing the following cost function

$$S(\mathbf{p}, \delta) = \sum_{m=1}^{M} 2\Re \left\{ p_m \mathbf{y}_m^{\mathrm{H}} \mathbf{s}(\delta) \right\} - |p_m|^2 \| \mathbf{s}(\delta) \|^2. \quad (15)$$

For any given δ, we can obtain the optimal solution of p_m that maximizes (15) with least square (LS) estimation

$$p_m = \frac{\mathbf{s}(\delta)^{\mathrm{H}} \mathbf{y}_m}{\| \mathbf{s}(\delta) \|^2}. \quad (16)$$

Substituting (16) into (15) yields the cost function for δ

$$\hat{\delta} = \underset{\delta}{\arg\max} \sum_{m=1}^{M} \frac{|\mathbf{s}(\delta)^{\mathrm{H}} \mathbf{y}_m|^2}{\| \mathbf{s}(\delta) \|^2}. \quad (17)$$

This estimation is performed through two steps: orthogonal matching pursuit (OMP) and Newtonized refinement (NR)

steps. We refer to the entire step sequence as one NOMP iteration. In the OMP step, we build a finite discrete set for δ

$$\boldsymbol{\Omega} = \left\{ k\left(\frac{2\pi}{\gamma N}\right) : k = 0, 1, \cdots, \gamma N - 1 \right\} \qquad (18)$$

where γ is the over-sampling rate relative to the grid. The rough solution of δ is found by substituting all the elements of set $\boldsymbol{\Omega}$ into (17), and the relative solution of $\mathbf{p}$ is obtained by substituting $\hat{\delta}$ into (16) for every m. In the NR step, we use Newton's method to iteratively refine the rough solution of δ to avoid the off-grid effect. The $(i+1)$-th refinement iteration calculates

$$\hat{\delta}^{i+1} = \hat{\delta}^i - \frac{\dot{S}(\hat{\mathbf{p}}^i, \hat{\delta}^i)}{\ddot{S}(\hat{\mathbf{p}}^i, \hat{\delta}^i)} \qquad (19)$$

where $(\hat{\mathbf{p}}^i, \hat{\delta}^i)$ is the refined result from the i-th iteration, and $\dot{S}(\mathbf{p}, \delta)$ and $\ddot{S}(\mathbf{p}, \delta)$ are the first and second partial derivative of $S(\mathbf{p}, \delta)$ with respect to δ, which are

$$\dot{S}(\mathbf{p}, \delta) = \sum_{m=1}^{M} \Re\left\{ (\mathbf{y}_m - p_m \mathbf{s}(\delta))^{\mathrm{H}} p_m \frac{\partial \mathbf{s}(\delta)}{\partial \delta} \right\}, \qquad (20)$$

$$\ddot{S}(\mathbf{p}, \delta) = \sum_{m=1}^{M} \Re\left\{ (\mathbf{y}_m - p_m \mathbf{s}(\delta))^{\mathrm{H}} p_m \frac{\partial^2 \mathbf{s}(\delta)}{\partial \delta^2} \right\}$$
$$- |p_m|^2 \left\| \frac{\partial \mathbf{s}(\delta)}{\partial \delta} \right\|^2. \qquad (21)$$

The relative solution of $\hat{\mathbf{p}}^{i+1}$ is obtained when substituting $\hat{\delta}^{i+1}$ into (16).

After t iterations of refinement, we denote $(\hat{\mathbf{p}}^t, \hat{\delta}^t)$ as $(\hat{\mathbf{p}}_1, \hat{\delta}_1)$ to represent the estimation of the first response. We obtain the residual channel by reducing the CFR of the first response from the channel

$$\mathbf{Y}_{\mathrm{r}} = \mathbf{Y} - \mathbf{s}(\hat{\delta}_1)\hat{\mathbf{p}}_1, \qquad (22)$$

where

$$\mathbf{Y} = [\mathbf{y}_1, \mathbf{y}_2, \cdots, \mathbf{y}_M]. \qquad (23)$$

Thus, we finish the first iteration of NOMP. The residual responses are determined by repeating the OMP and NR steps with $(J-1)$ iterations, but the following NR step is slightly different from the first iteration. Given that a single response estimation in an iteration is affected by the previous iteration and the residual responses in the channel, once we estimate a new response, we cyclic refine each estimated response again by using the NR step. Whenever we remove the estimated responses at the end of the iteration, we refine $\hat{\mathbf{P}}$ with LS estimation

$$\hat{\mathbf{P}} = \left[\mathbf{S}(\hat{\boldsymbol{\delta}})^{\mathrm{H}} \mathbf{S}(\hat{\boldsymbol{\delta}})\right]^{-1} \mathbf{S}(\hat{\boldsymbol{\delta}})^{\mathrm{H}} \mathbf{Y}, \qquad (24)$$

at the t-th NOMP iteration, where

$$\mathbf{S}(\hat{\boldsymbol{\delta}}) = \left[\mathbf{s}(\hat{\delta}_1), \mathbf{s}(\hat{\delta}_2), \cdots, \mathbf{s}(\hat{\delta}_t)\right]. \qquad (25)$$

This LS refinement ensures that the power of the residual signal is minimized.

After estimating $(\mathbf{P}, \boldsymbol{\delta})$ from every angle, we normalize $\mathbf{P}$ and align $\boldsymbol{\delta}$ to obtain the synthesized antenna response for every angle. We assume that δ_1 is almost equal to τ, so we

obtain ϕ_j with

$$\hat{\phi}_j = \delta_j - \delta_1, \ \forall j \qquad (26)$$

at every angle. In addition, we obtain $r_{m,j}$ with

$$\hat{r}_{m,j} = \frac{p_{m,j}}{\sqrt{\sum_{m'=1}^{M} \sum_{j'=1}^{J} |p_{m',j'}|^2}}, \ \forall m, j. \qquad (27)$$

The measured antenna response $a_{\mathrm{PRA},m}(\theta)$ is finally obtained by substituting (26) and (27) into (5). We gather the gain, delay, and phase (GDP) of the antenna responses for every angle, i.e., (26) and (27), into a table, termed the GDP table. In the online stage, we use the GDP table to synthesize a steering vector to identify AoAs from cluttering multipath parameters.

B. Online Stage: ToA and AoA Estimation

In the online stage, the signal is received through the multipath channel as given by (1). We stack the received signals of N subcarriers and M antennas and express the multipath CFR as a vector form

$$\mathbf{h} = [h_{1,1}, \ldots, h_{N,1}, \ldots, h_{1,M}, \ldots, h_{N,M}]^{\mathrm{T}},$$
$$= \sum_{l=1}^{L} g_l \mathbf{v}(\tau_l, \theta_l), \qquad (28)$$

where

$$\mathbf{v}(\tau, \theta) = \mathbf{a}(\theta) \otimes \mathbf{s}(\tau) \qquad (29)$$

with $\otimes$ being the Kronecker product and

$$\mathbf{a}(\theta) = [a_1(\theta), a_2(\theta), \cdots, a_M(\theta)]^{\mathrm{T}}. \qquad (30)$$

Here, $\mathbf{a}(\theta)$ is the *synthesized* steering vector with the antenna response $a_m(\cdot)$ given by (5), and we have removed the subscript "PRA" from $a_m(\cdot)$ and $\mathbf{a}(\cdot)$ to make the notation concise. Accordingly, the received signal vector is now modeled as

$$\mathbf{y} = \sum_{l=1}^{L} g_l \mathbf{v}(\tau_l, \theta_l) + \mathbf{z}. \qquad (31)$$

The ML estimation for online stage is

$$\left(\hat{\mathbf{g}}, \hat{\boldsymbol{\tau}}, \hat{\boldsymbol{\theta}}\right) = \underset{\mathbf{g}, \boldsymbol{\tau}, \boldsymbol{\theta}}{\operatorname{argmin}} \left\| \mathbf{y} - \sum_{l=1}^{L} g_l \mathbf{v}(\tau_l, \theta_l) \right\|^2, \qquad (32)$$

where

$$\hat{\mathbf{g}} = [\hat{g}_1, \hat{g}_2, \cdots, \hat{g}_L], \qquad (33)$$

$$\hat{\boldsymbol{\tau}} = [\hat{\tau}_1, \hat{\tau}_2, \cdots, \hat{\tau}_L], \qquad (34)$$

$$\hat{\boldsymbol{\theta}} = \left[\hat{\theta}_1, \hat{\theta}_2, \cdots, \hat{\theta}_L\right]. \qquad (35)$$

We still first consider single path estimation, so the ML estimation of one path can be represented as

$$\left(\hat{g}, \hat{\tau}, \hat{\theta}\right) = \underset{g, \tau, \theta}{\operatorname{argmin}} \|\mathbf{y} - g\mathbf{v}(\tau, \theta)\|^2. \qquad (36)$$

The solution of (36) can be obtained when maximizing the following cost function

$$S(g, \tau, \theta) = 2\Re\left\{\mathbf{y}^{\mathrm{H}} g\mathbf{v}(\tau, \theta)\right\} - |g|^2 \|\mathbf{v}(\tau, \theta)\|^2. \qquad (37)$$

For any given τ and θ, we can obtain the optimal solution of g that maximize (37) with LS estimation

$$\hat{g} = \frac{\mathbf{v}(\tau,\theta)^{\mathrm{H}}\mathbf{y}}{\|\mathbf{v}(\tau,\theta)\|^2} \tag{38}$$

Substituting (38) into (37) yields the cost function for (τ,θ)

$$(\hat{\tau},\hat{\theta}) = \operatorname*{argmax}_{\tau,\theta} \frac{\left|\mathbf{v}(\tau,\theta)^{\mathrm{H}}\mathbf{y}\right|^2}{\|\mathbf{v}(\tau,\theta)\|^2}. \tag{39}$$

This estimation is also performed through the OMP and NR steps similar to those in Section III.A with a slight variant. In the OMP step, the rough solutions of τ and θ are found by substituting subsets from $\mathbf{\Omega}$ and the synthesized steering vector from the GDP table into (39), and the relative solution of g is obtained when substituting $(\hat{\tau},\hat{\theta})$ into (38). Given that the synthesized steering vector cannot be written as an analytic function, we cannot obtain the partial derivative of $S(g,\tau,\theta)$ with respect to θ. Therefore, in the NR step, we only refine $\hat{\tau}$ with Newton's method

$$\hat{\tau}^{i+1} = \hat{\tau}^i - \frac{\dot{S}(\hat{g}^i,\hat{\tau}^i,\hat{\theta}^i)}{\ddot{S}(\hat{g}^i,\hat{\tau}^i,\hat{\theta}^i)}, \tag{40}$$

where $(\hat{g}^i,\hat{\tau}^i,\hat{\theta}^i)$ is the refined result of the i-th iteration, and $\dot{S}(g,\tau,\theta)$ and $\ddot{S}(g,\tau,\theta)$ are the first and second partial derivative of $S(g,\tau,\theta)$ with respect to τ, respectively. Then, we substitute $\hat{\tau}^{i+1}$ and the antenna response from the measured dataset into (39) to refine θ and obtain $\hat{\theta}^{i+1}$. Finally, we substitute $(\hat{\tau}^{i+1},\hat{\theta}^{i+1})$ into (38) to obtain $\hat{g}^{i+1}$.

After t iterations of refinement, we denote $(\hat{g}^t,\hat{\tau}^t,\hat{\theta}^t)$ as $(\hat{g}_1,\hat{\tau}_1,\hat{\theta}_1)$ to represent the estimation result of the first path. We calculate the residual channel by removing the CFR of the first path from the channel

$$\mathbf{y}_{\mathrm{r}} = \mathbf{y} - \hat{g}_1\mathbf{v}(\hat{\tau}_1,\hat{\theta}_1). \tag{41}$$

The residual paths are obtained by repeating the NOMP iterations. Before reducing the estimated path, we refine $\hat{\mathbf{g}}$ with LS estimation

$$\hat{\mathbf{g}} = \left[\mathbf{V}(\hat{\boldsymbol{\tau}},\hat{\boldsymbol{\theta}})^{\mathrm{H}}\mathbf{V}(\hat{\boldsymbol{\tau}},\hat{\boldsymbol{\theta}})\right]^{-1}\mathbf{V}(\hat{\boldsymbol{\tau}},\hat{\boldsymbol{\theta}})^{\mathrm{H}}\mathbf{y} \tag{42}$$

at the t-th NOMP iteration,

$$\mathbf{V}(\hat{\boldsymbol{\tau}},\hat{\boldsymbol{\theta}}) = \left[\mathbf{v}(\hat{\tau}_1,\hat{\theta}_1),\mathbf{v}(\hat{\tau}_2,\hat{\theta}_2),\cdots,\mathbf{v}(\hat{\tau}_t,\hat{\theta}_t)\right]. \tag{43}$$

The iteration stops when the residual signal power is less than the threshold.

As mentioned in Section III.A, the estimation for a single path is also affected by the previous iteration and the residual paths in the channel. Remarkably, in the case of using the URA, a propagation path only causes one response on an antenna, so the interference between every iteration can be avoided by using the cyclic NR step. However, the phone antenna elicits multiple responses as shown in Figure 1(b). If the antenna responses of a propagation path do not be completely removed in an iteration, the extra responses would cause serious interference in the estimation of other paths in the online stage. Therefore, exhausting all the components of the antenna response at every angle in the offline stage is
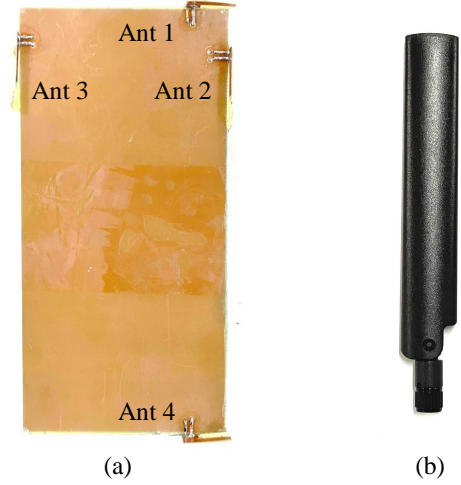

Fig. 3: Antennas used in the measurement. (a) Ground plane with four antennas equipped at Rx. (b) Omnidirectional antenna equipped at Tx.

crucial.

IV. EXPERIMENTS AND DISCUSSIONS

In this section, we conduct experiments and simulations to evaluate the proposed AoA estimation algorithms. To imitate a real phone, we develop four antennas following the form factor of a mobile phone, as shown in Figure 3(a). The size of the ground plane is the same as a smartphone 8 mm thick with a 6.22 inch screen. The spacing between two adjacent antennas is different. If we set (m_x,m_y) of antenna 1 as $(0,0)$, (m_x,m_y) of antennas $2-4$ are $(0.1898,-0.33)$, $(-1.5,-0.2)$, and $(0,-3.77)$, respectively. In both the measurements and the simulations, the OFDM-based 5G NR waveform is used with the maximum available channel bandwidth at 3.9 GHz, i.e., frequency range 1. A channel bandwidth of 100 MHz with subcarrier spacing of 60 kHz is used. Specifically, we consider an NR frequency-domain resource grid with $N = 1,644$ active subcarriers in one OFDM symbol.

We gather the measured antenna responses at every angle by using the technique in Section III.A in an anechoic chamber. Then, we use the established GDP table to estimate AoAs in a classroom. We also combine the GDP table with ray-tracing Wireless InSite® [36] software to synthesize multipath channels in an office, allowing us to evaluate the proposed algorithms in a big environment.

A. Continuity of Antenna Responses

In this paper, we measure the antenna responses of the phone antennas at azimuth $0°,1°,2°,\ldots,359°$ and elevation $0°,5°,10°,\ldots,30°$ and gather total $2,520$ angles into the GDP table. However, we find that this offline measurement stage can be done more efficiently by using the continuity property of the antenna responses.

To illustrate this property, we show in Figure 4 the magnitude and phase of the measured steering vector at 11 continuous azimuths. We observe that the antenna responses in (3) are
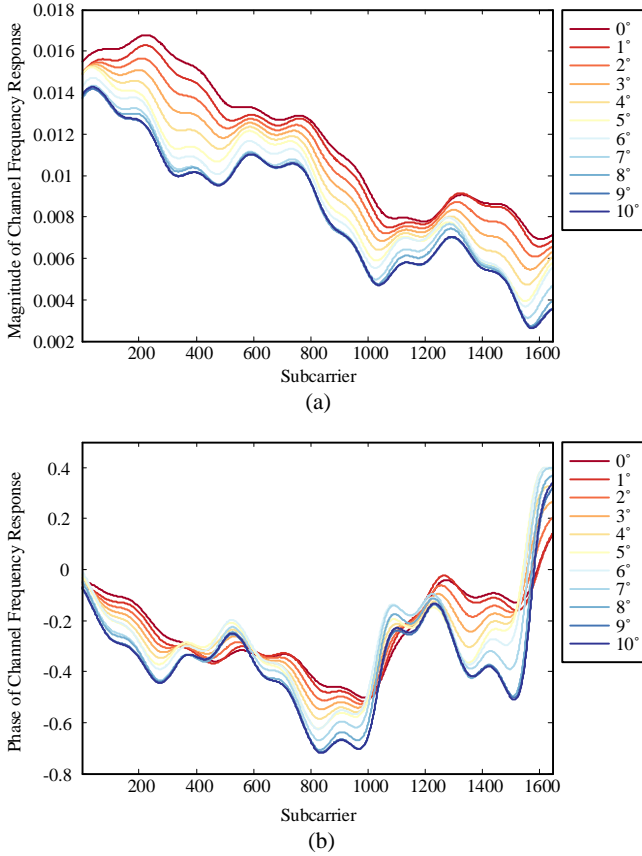
Fig. 4: (a) Magnitudes and (b) phases of the CFRs at 11 continuous azimuths.

continuous at every angle. The continuity property only can be observed *after aligning the initial phase of every measurement*. Taking advantage of this continuous property, we can measure the CFRs in a wider azimuth spacing and interpolate the CFRs for other azimuths to save the data collection time in the offline stage. With the CFRs for other azimuths, we can obtain the artificial antenna responses of these azimuths by using the parameter extracting technique in Section III.A.

Using the measurements of every $5°$ of azimuth and the interpolated results, we evaluate the AoA estimation performance in the anechoic chamber. The estimation error at every angle is less than $2°$. The result demonstrates that the performance with the interpolate method remains relatively good, while the time for establishing the lookup table can be significantly reduced. The saving of the offline stage also means that the calibration time of a phone in a factory can be reduced.

B. Measurement Results

The measurements were conducted in an indoor classroom, at the National Sun Yat-sen University, Taiwan, as shown in Figure 5. The classroom is approximately $9.5\,m \times 9.6\,m$ with a ceiling height of $2.9\,m$. To easily move the instruments, we put all the desks against the wall. We use an SGT100A radio frequency vector signal generator equipped with a single omnidirectional antenna in Figure 3(b) as Tx and fix it in the

middle of the classroom. The height of the Tx antenna is 1.6 m. We use an RTO2000 digital oscilloscope equipped with the phone antennas in Figure 3(a) as Rx and make the Rx movable. The height of the Rx antenna is $1.23\,m$. The measurements are conducted with a distance step of $1\,m$ between two adjacent Rx points and provide a total of 64 sets of measurements. For ease of reference, the row is indexed by $A, B, \ldots, H$, while the column is indexed by $1, 2, \ldots, 8$. If we set the coordinate of the lower-left corner of the classroom as $(0\,m, 0\,m)$, then the coordinate of the Rx point A1 is $(1.2\,m, 8.4\,m)$. Given that we perform the synchronization through the synchronization signal in 5G NR, the estimated ToA has clock bias and is not the true ToA of the propagation path. Therefore, in the following measurements, we only discuss the performance of the AoA estimation.

We repeat the measurement process 200 times at each Rx point and show the estimation results in Figure 6. Figure 6(a) shows the average SNR of the four antennas. When the Rx is closer to the Tx, the Rx has the higher SNR. We pick the strongest estimated path as the LoS path and show the average estimation error of azimuth AoA in Figure 6(b). We find significant errors when the Rx points are near the walls. The reasons for this effect are two reasons. First, the delay between the LoS signal and reflected signals from walls and desks are moving closer; the two paths might be estimated as the same path and cause estimation error on the LoS AoA. Second, when the power of the LoS signal becomes lower and the estimated gain of the reflected signal is comparable to the LoS signal, we could not distinguish the LoS signal. Figure 6(b) also shows significant errors of certain Rx points that are not near the walls, such as B3 and C6. This error is due to the similarity of the antenna responses. To reflect this effect, we calculate the correlation value

$$R(\hat{\theta}_1, \theta_1) = |a_m^*(\hat{\theta}_1)a_m(\theta_1)| \qquad (44)$$

where $\hat{\theta}_1$ is the estimated LoS AoA and θ_1 is the ground truth LoS AoA. If $R(\hat{\theta}_1, \theta_1)$ is close to one but $\hat{\theta}_1 \neq \theta_1$, then estimation ambiguity will occur. Figure 6(c) shows the correlation values of every estimated LoS azimuth AoA and ground truth LoS azimuth AoA at elevation $0°$. For example, $\theta_1 = 180°$ is easily ambiguous with $\hat{\theta}_1 = 270°$. The correlation value of the steering vector of these two angles is 0.96. The ambiguity also exists between different elevations.

To corroborate the importance of the established GDP table, we compare the AoA estimation performances over three different lookup tables: the 3D GDP table, the two-dimensional (2D) GDP table, and the formula 3D table. The 3D GDP table is obtained through the proposed procedures presented in Section IV.A. The 2D GDP table is obtained from the 3D GDP table by extracting the antenna responses in elevation $0°$. The formula 3D table is obtained by substituting the positions of the antennas, that is, (m_x, m_y), into (2). Compared with the 3D GDP table, the formula 3D table only reflect the phase differences between antenna elements and does not consider the practical antenna responses, such as the different amplitude and delay responses among antennas. We calculate the LoS azimuth AoA estimation error with
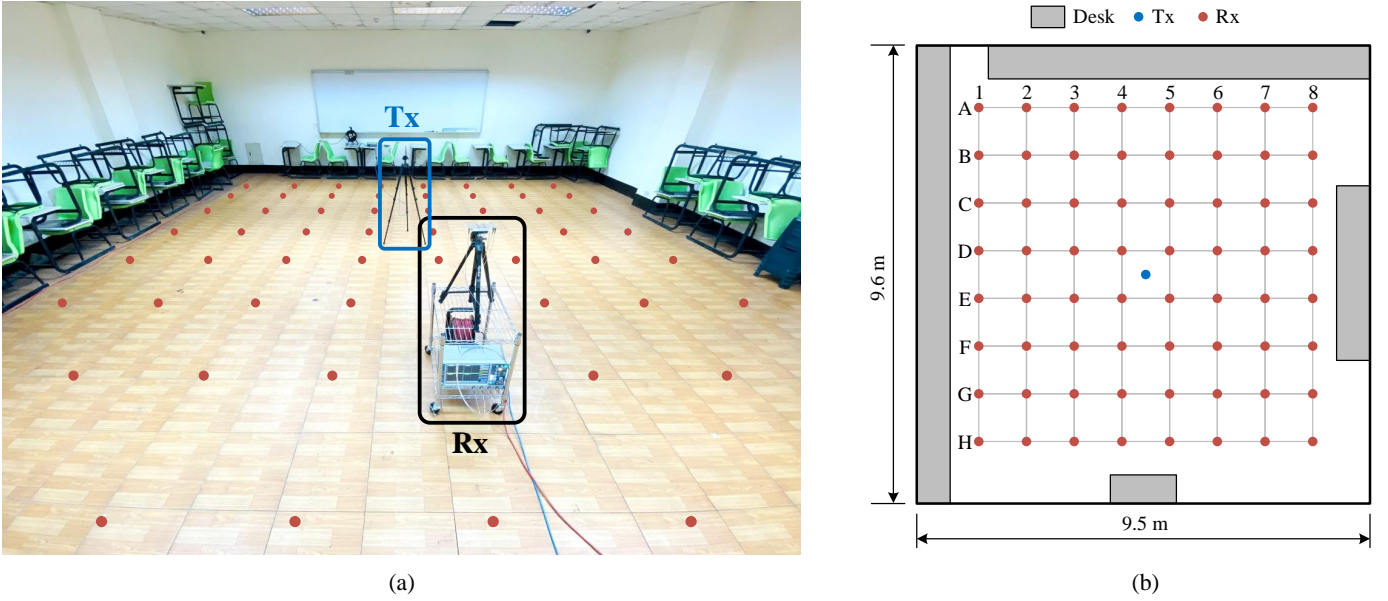
(a)

(b)

Fig. 5: Measurement area in a classroom at the National Sun Yat-sen University. (a) Overview. (b) Layout.
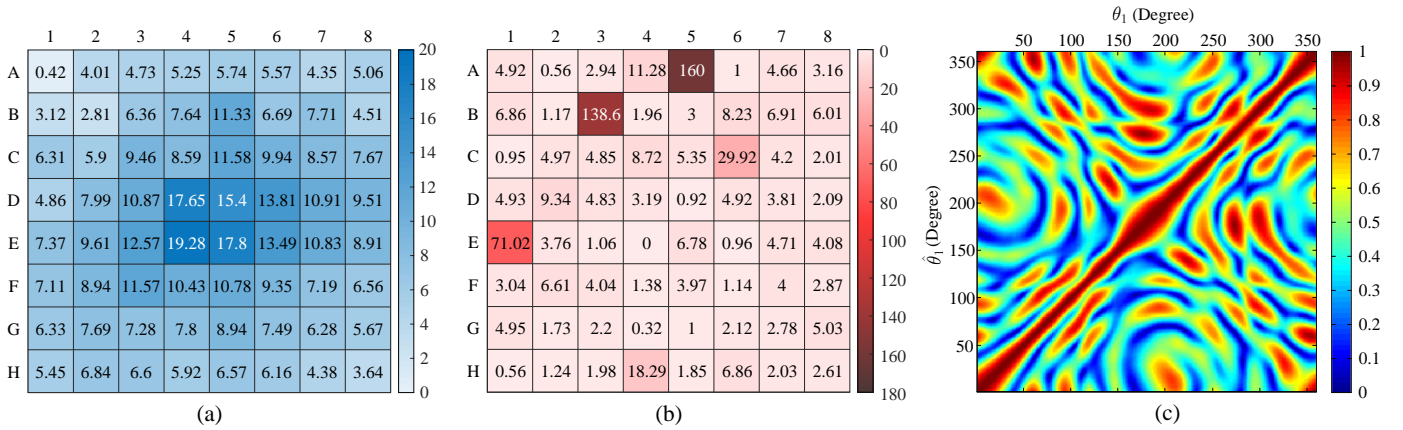

(a)

(b)

(c)

Fig. 6: Estimation results of the phone antennas (a) Average SNR (dB). (b) Average estimation error (degrees) of LoS azimuth AoA. (c) Ambiguity of the estimated LoS azimuth AoA and ground truth LoS azimuth AoA at elevation 0°.
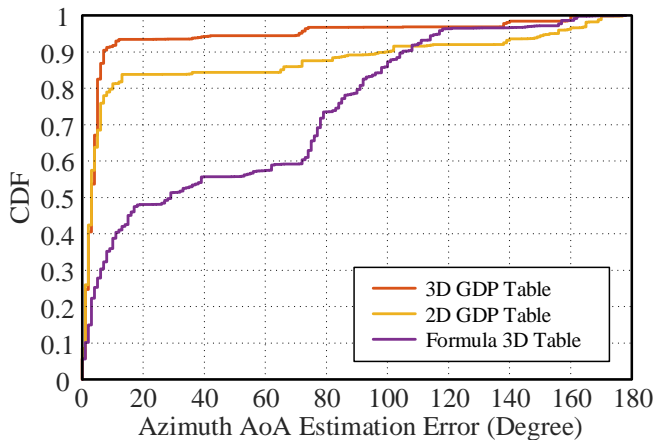

Fig. 7: CDF of azimuth AoA estimation error.

the three tables for the 200 measurements at every Rx point and present the cumulative distribution function (CDF) of estimation error in Figure 7. We can observe that the 3D GDP table achieves the highest accuracy, with 82.5% and 91.8% probabilities that the errors are lower than 5° and 10°, respectively. The 2D GDP table ignores the elevation AoAs resulting in performance degeneration. Specifically, for the 2D GDP table, the probability that the errors are lower than 5° and 10° are 68.5% and 81.3%, respectively. The formula 3D table has the worst performance because it completely ignores the effects of antenna responses, resulting in probabilities of only 27.9% and 38.8% that the errors are lower than 5° and 10°, respectively.

Next, we evaluate the AoA estimation performance under a moving scenario. We move the Rx along three straight line trajectories: from A8 to H8 in path 1, from A7 to H7 in path 2, and from A6 to H6 in path 3. To obtain the ground-truth
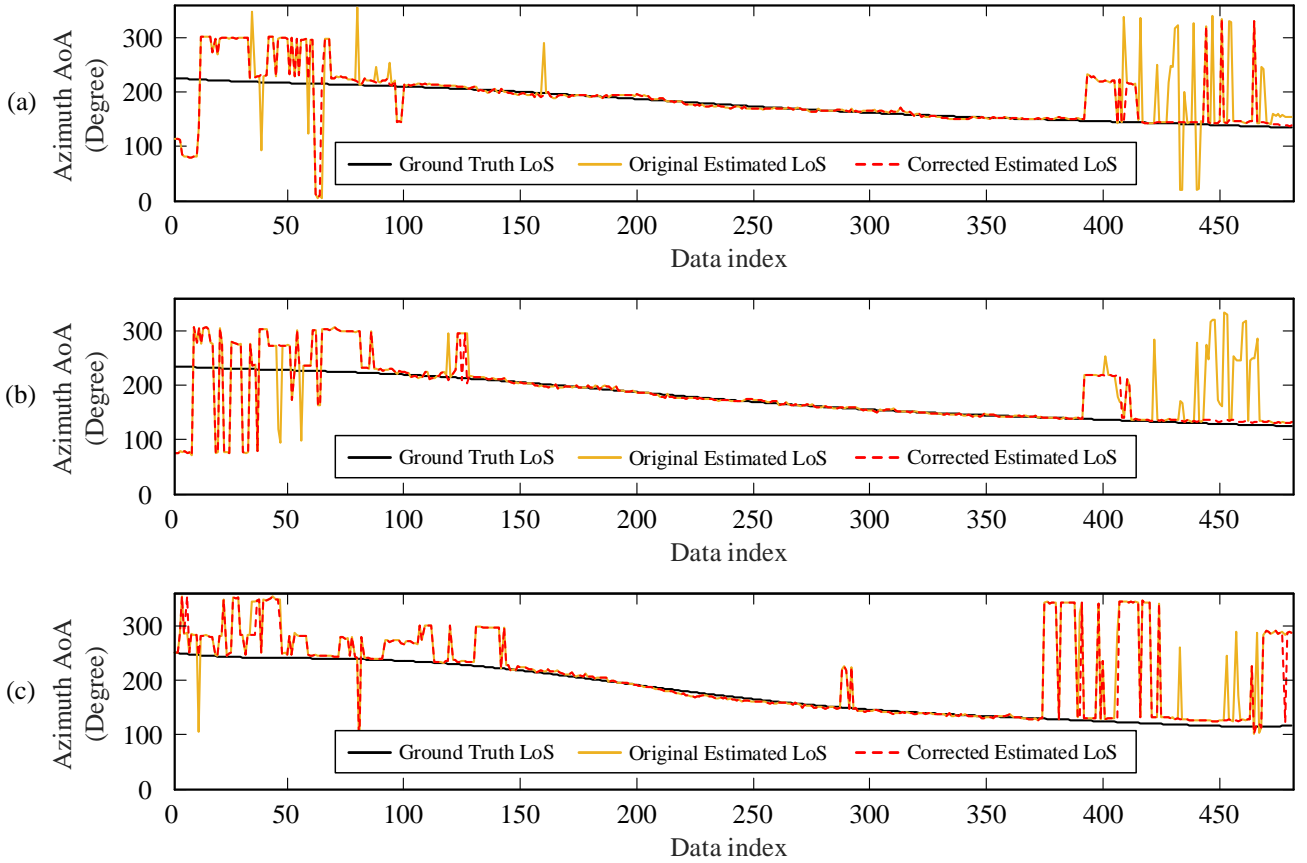
Fig. 8: Ground truth, original estimated, and corrected estimated LoS azimuth AoA on the (a) path 1 (b) path 2 and (c) path 3.

AoAs, we attempt to maintain a constant speed during the movement. The estimation results of the three trajectories are shown in Figure 8. Except for a few clustered errors appearing in certain segments, the estimation results (yellow solid line) correspond to the ground truths (black solid line) in most of the cases. We find significant estimation errors at the beginning and end of the three paths, which result from the fact that the Rx moves close to the walls and desks, thereby receiving many reflections. We analyze these estimated AoAs and realize that some of the reflections have a larger path gain than the LoS path, thereby resulting in the LoS identification error. This phenomenon is reasonable because the practical phone antenna may have different magnitude responses for different AoAs. The LoS path might not always correspond to the strongest path, especially when the LoS path and the reflection path have similar traveling distances. Therefore, we identify the LoS path with the aid of ToA. Specifically, when the second estimated path has a shorter delay than the first estimated path, we choose the second estimated path to be the LoS path. Given this modification, we find that some of the estimation errors (red dashed line) can be corrected. For example, many estimation errors are corrected for the data indexes from 400 to the end of the three trajectories. Other estimation errors might result from the ambiguity of the steering vector. For example, we have mentioned in Figure 6(b) that phase ambiguity occurs around area C6. Therefore, when Rx is passing through the

area around C6, corresponding to the data indexes from 90 to 150 in path 3, considerable amounts of estimation error occur.

C. Simulation Results

To understand the performances of the proposed methods in wide scenarios, we combine the 3D GDP table with the realistic ray-tracing simulations obtained by Wireless InSite software. The layout in these simulations, which is an office with a ceiling height of $2.62\,\mathrm{m}$, is shown in Figure 9. The office has three types of walls, namely, a glass wall $3\,\mathrm{cm}$ thick, a wooden wall $6\,\mathrm{cm}$ thick, and concrete walls. The concrete wall in the middle of the office is $15\,\mathrm{cm}$ thick, and other concrete walls are $30\,\mathrm{cm}$ thick. The height of the wooden desks in the office is $0.75\,\mathrm{m}$. We set three Txs equipped with omnidirectional antennas on the ceiling in different locations: one is in a spacious place, and the others are set in a narrow corridor. The transmit power is 20 dBm. A total of $6,890$ Rx points are used with an antenna height of $1.2\,\mathrm{m}$, and the distance between two adjacent Rx points is $0.2\,\mathrm{m}$. The number of allowed interactions is limited to six reflections and five penetrations, and the number of received rays is limited to 250. When a signal transmits through a glass wall, wooden wall, or $15\,\mathrm{cm}$ thick concrete wall from the vertical direction of the wall, the signal attenuation is 0.15, 0.51, and 10.27 dB respectively. The default antennas in Wireless InSite do
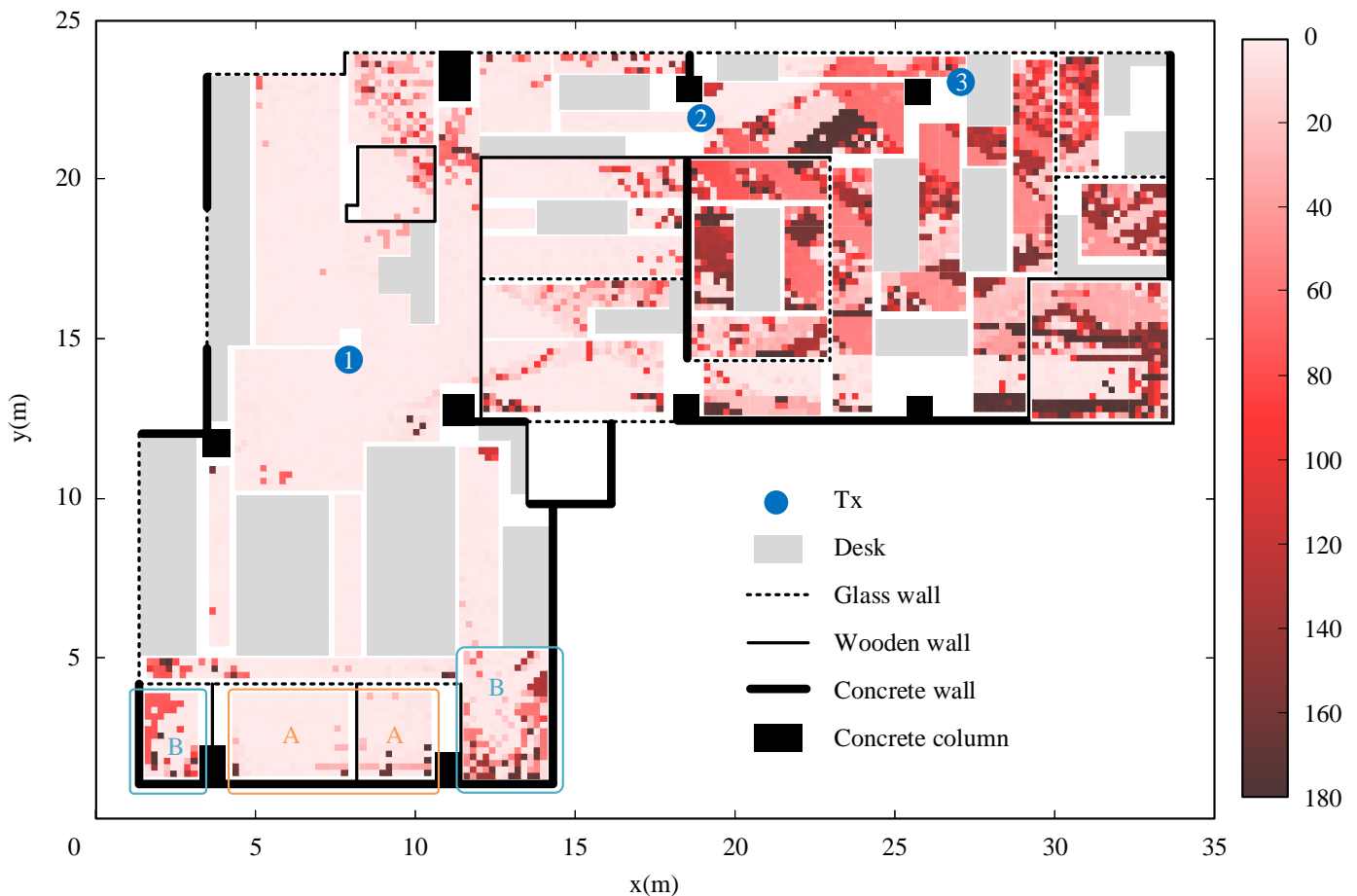
Fig. 9: AoA estimation error of the phone antennas when only using Tx 1.

not reflect the responses of the phone antenna. Given that the antenna responses are time-invariant systems, we substitute the 3D GDP table into (5) to generate the synthesized steering vector of the rays and obtain the CFRs of the phone antenna.

We fixed the noise power for all Rx points at a certain level, resulting in an SNR of approximately 15 dB near the Tx. The azimuth AoA estimation error of the phone antenna by using the 3D GDP table is shown in Figure 9. A darker color represents a larger estimation error. The error occurs is regardless of the clockwise or counterclockwise direction, so the minimum and maximum errors are 0° and 180°. As the distance increases, the error becomes larger. Furthermore, the Rx points near the walls have significant errors. These phenomena are consistent with the measurement results. We also evaluate the estimation performance with the 3D GDP table, the 2D GDP table, and the formula 3D table. In addition, we consider the fourth lookup table: a phone with four *ideal* isotropic antennas. An ideal isotropic antenna elicits only one response from a single-path signal, and the power of the antenna response is equal at every angle. The ideal isotropic antenna can be regarded as the benchmark of a phone antenna in terms of communication performance. We generate the channel for the ideal antennas and evaluate the estimation performance with the formula 3D table.

We evaluate the performance of the estimated azimuth AoA

for the four lookup tables at four specific scenarios. Table I shows the corresponding results, namely, the probabilities that the errors are lower than 5° and 10°. In the following descriptions, we simply call "the probabilities that the errors are lower than 5° and 10°" the probabilities. In the first three scenarios, we only consider those Rx points that the LoS signal is the strongest power among the multipath. Scenario 1 considers the cases under different Tx-Rx distances when Tx 1 is used to transmit the signal. Given that Tx 1 is located at a spacious place, and the area within 10 m has fewer obstacles and walls, this area has the highest probability. In the area beyond 10 m, the power of the LoS signal remains the largest yet has decreased during the transmission and penetration, finally becoming similar to the reflected signal. Thus, this area has a lower probability.

Similar to scenario 1, scenario 2 considers using Tx 2 to transmit the signal. Tx 2 is located in a narrow corridor between a concrete column and a wooden wall. After penetrating the wooden wall, the signal encounters a concrete wall. These obstacles result in similar ToA paths with the LoS path and cause many errors in the area within 10 m. In the area beyond 10 m, especially the spacious area near Tx 1, the ToAs between the LoS signal and the reflected signals are large. Therefore, this area, on the contrary, has higher probability. These two scenarios allow us to conclude that although the estimation

TABLE I: Probabilities of estimation error less than 5°/10° for four simulated methods.

Antenna Type		Phone			Ideal
Table		GDP		Formula	Formula
Dimension		3D	2D	3D	3D
Tx 1	$d \le 10$m	89 / 92	63 / 70	57 / 61	**90** / 92
	$d > 10$m	**72 / 76**	61 / 67	56 / 62	70 / 73
Tx 2	$d \le 10$m	**74 / 83**	56 / 66	41 / 51	72 / 80
	$d > 10$m	**80 / 86**	73 / 80	60 / 70	78 / 85
Tx 1	Area A	**91 / 92**	86 / 88	75 / 77	90 / 90
	Area B	**60 / 63**	45 / 47	16 / 17	39 / 43
Tx 3	$d \le 10$m	**67 / 71**	66 / 70	47 / 58	63 / 68

TABLE II: Probabilities of estimation error less than 5°/10° for different bandwidth.

Bandwidth		100 MHz	50 MHz	20 MHz
Tx 1	$d \le 10$m	**89 / 92**	84 / 88	75 / 81
	$d > 10$m	**72 / 76**	57 / 64	45 / 53
Tx 2	$d \le 10$m	**74 / 83**	67 / 78	59 / 71
	$d > 10$m	**80 / 86**	72 / 80	61 / 71
Tx 1	Area A	**91 / 92**	76 / 80	57 / 63
	Area B	**60 / 63**	39 / 47	31 / 38
Tx 3	$d \le 10$m	**67 / 71**	58 / 64	48 / 55

performance is affected by the distance and SNR, the reflection paths caused by obstacles have a greater effect.

To prove this argument, in scenario 3, we use Tx 1 to observe the Rx points in two areas with $d > 10$ m. These areas are marked as areas A and B in Figure 9. Although area A and part of area B are blocked by the glass walls, the LoS signal is almost unaffected because the signal attenuation caused by the signal passing through the glass wall is very small. In this case, area A is mainly affected by the reflection of one concrete wall, and area B is affected by the reflection of two concrete walls. With dense reflection signals, the LoS estimation performance is much worst in area B.

In scenario 4, we use Tx 3 to transmit the signal. Tx 3 is located next to a concrete column, so the LoS signal of most Rx points is blocked by the column, and the power of the LoS signal is seriously attenuated. In the scenario, we only consider those Rx points whose LoS signals do not have the strongest power among the multipath within 10 m. Although we cannot calculate the azimuth AoA estimation error of the LoS signal, we can still calculate the azimuth AoA estimation error of the signal with the strongest power among the multipath.

From Table I, we further observe that the AoA estimation performance of the phone antenna with the 3D GDP table is better than that with the measured 2D and formula 3D tables and even slightly better than that with the ideal antennas. The reason for this finding is that the steering vector of the phone antennas has different amplitude responses among different antennas, so the similarity of the steering vector of the phone antenna at different angles is lower than that of the ideal antenna. We calculate the correlation value of the steering vector at every angle for the phone antennas and the ideal
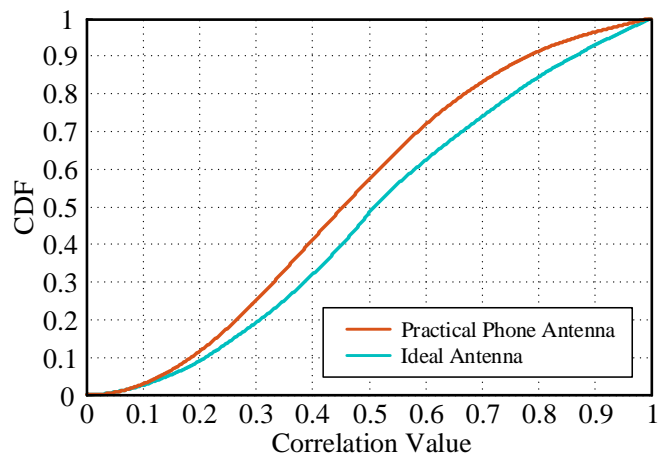

Fig. 10: CDF of correlation value of the steering vector at every angle.

antennas and show the CDF of the correlation value in Figure 10. Consequently, although the practical phone antennas lead to annoying antenna responses and thus challenge the AoA estimation, this effect is not always a disadvantage to AoA estimation.

Finally, we evaluate the performance of the phone antenna with the 3D GDP table for different bandwidths. Given that the subcarrier spacing is fixed at 60 kHz, we simulate a channel bandwidth of 50 MHz with $N = 816$ active subcarriers, and a channel bandwidth of 20 MHz with $N = 512$ active subcarriers. As shown in Table II, the large bandwidth also allows for a better AoA estimation accuracy, and we observe an approximately 10% area improvement with each doubling of the bandwidth.

V. Conclusion

Antenna configurations in practical mobile handsets do not conform to the idealization of zero spatial correlation between antennas and zero mutual coupling, and the actual antenna responses are highly complex but their impact on localization performance is not well understood. Motivated by this, this paper proposed a generic parameteric model that incorporates the actual antenna responses into AoA estimation. A two-stage algorithm was developed for efficient 3D AoA estimation for mobile devices. During the offline stage, the parameters of the antenna model were extracted at every angle in the anechoic chamber and gathered into a table. Then in the online stage, we used this table to synthesize the steering vectors and applied them to estimate the AoAs from the multipath channel. Using the proposed algorithm, we implemented it on a 5G NR mobile phone at 3.9GHz band with 100MHz channel bandwidth and assessed the estimation performance through experiments and extensive ray tracing-based simulations. The results confirmed great performance of the proposed and revealed that complex antenna responses actually helped diversify the steering vector between every angle for reducing ambiguity.

REFERENCES

[1] S. Bartoletti, A. Conti, D. Dardari, and A. Giorgetti, "5G localization and context-awareness," 2018. [Online]. Available: https://www.5gitaly.eu/2018/en/white-ebook-2/

[2] Y. Li *et al.*, "Toward location-enabled IoT (LE-IoT): IoT positioning techniques, error sources, and error mitigation," *IEEE Internet Things J.*, vol. 8, no. 6, pp. 4035–4062, 2021.

[3] A. Al-Fuqaha, M. Guizani, M. Mohammadi, M. Aledhari, and M. Ayyash, "Internet of Things: A survey on enabling technologies, protocols, and applications," *IEEE Commun. Surveys Tuts.*, vol. 17, no. 4, pp. 2347–2376, 2015.

[4] F. Zafari, A. Gkelias, and K. K. Leung, "A survey of indoor localization systems and technologies," *IEEE Commun. Surveys Tuts.*, vol. 21, no. 3, pp. 2568–2599, 2019.

[5] S. Sadowski and P. Spachos, "RSSI-based indoor localization with the Internet of Things," *IEEE Access*, vol. 6, pp. 30 149–30 161, 2018.

[6] L. Chen, I. Ahriz, and D. Le Ruyet, "AoA-aware probabilistic indoor location fingerprinting using channel state information," *IEEE Internet Things J.*, vol. 7, no. 11, pp. 10 868–10 883, 2020.

[7] Y. Zhao, Z. Zhang, T. Feng, W.-C. Wong, and H. K. Garg, "GraphIPS: Calibration-free and map-free indoor positioning using smartphone crowdsourced data," *IEEE Internet Things J.*, vol. 8, no. 1, pp. 393–406, 2021.

[8] B. Huang, Z. Xu, B. Jia, and G. Mao, "An online radio map update scheme for WiFi fingerprint-based localization," *IEEE Internet Things J.*, vol. 6, no. 4, pp. 6909–6918, 2019.

[9] C. Wu, F. Zhang, B. Wang, and K. J. R. Liu, "EasiTrack: Decimeter-level indoor tracking with graph-based particle filtering," *IEEE Internet Things J.*, vol. 7, no. 3, pp. 2397–2411, 2020.

[10] J. Choi and Y. Choi, "Calibration-free positioning technique using Wi-Fi ranging and built-in sensors of mobile devices," *IEEE Internet Things J.*, vol. 8, no. 1, pp. 541–554, 2021.

[11] Y. Li, X. Hu, Y. Zhuang, Z. Gao, P. Zhang, and N. El-Sheimy, "Deep reinforcement learning (DRL): Another perspective for unsupervised wireless localization," *IEEE Internet Things J.*, vol. 7, no. 7, pp. 6279–6287, 2020.

[12] R. Liu *et al.*, "Collaborative SLAM based on WiFi fingerprint similarity and motion information," *IEEE Internet Things J.*, vol. 7, no. 3, pp. 1826–1840, 2020.

[13] X. Li, E. Leitinger, and F. Tufvesson, "RSS-based localization of low-power IoT devices exploiting AoA and range information," in *Proc. 54th Asilomar Conf. Signals, Syst., and Comput. (ACSSC)*, 2020, pp. 651–656.

[14] P. H. Pathak, X. Feng, P. Hu, and P. Mohapatra, "Visible light communication, networking, and sensing: A survey, potential and challenges," *IEEE Commun. Surveys Tuts.*, vol. 17, no. 4, pp. 2047–2077, 2015.

[15] B. Lin *et al.*, "Experimental demonstration of optical camera communications based indoor visible light positioning system," in *Proc. 16th Int. Conf. Opt. Commun. Netw. (ICOCN)*, 2017, pp. 1–3.

[16] IEEE P802.11Task Group AZ, "Status of IEEE 802.11az next generation positioning (NGP)," 2021. [Online]. Available: https://www.ieee802.org/11/Reports/tgaz_update.htm

[17] 3GPP, "LTE; 5G; LTE positioning protocol (lpp)," 3rd Generation Partnership Project (3GPP), Technical Specification (TS) 37.355, Jan 2020, version 15.0.0.

[18] 3GPP, "5G; NG radio access network (NG-RAN); Stage 2 functional specification of User Equipment (UE) positioning in NG-RAN," 3rd Generation Partnership Project (3GPP), Technical Specification (TS) 38.305, Jul. 2020, version 16.1.0.

[19] Z. Chaloupka, "Technology and standardization gaps for high accuracy positioning in 5G," *IEEE Commun. Standards Mag.*, vol. 1, no. 1, pp. 59–65, 2017.

[20] J. Xiong and K. Jamieson, "ArrayTrack: A fine-grained indoor location system," in *Proc. 10th USENIX Symp. Netw. Syst. Des. Implement. (NSDI)*, 2013, pp. 71–84.

[21] M. Kotaru, K. Joshi, D. Bharadia, and S. Katti, "SpotFi: Decimeter level localization using WiFi," in *Proc. 2015 ACM Conf. Spec. Interest Group Data Commun. (SIGCOMM)*, 2015, pp. 269–282.

[22] W. Gong and J. Liu, "RoArray: Towards more robust indoor localization using sparse recovery with commodity WiFi," *IEEE Trans. Mobile Comput.*, vol. 18, no. 6, pp. 1380–1392, 2019.

[23] F. Han, C. Wan, P. Yang, H. Zhang, Y. Yan, and X. Cui, "ACE: Accurate and automatic CSI error calibration for wireless localization system," in *Proc. 6th Int. Conf. Big Data Comput. Commun. (BIGCOM)*, 2020, pp. 15–23.

[24] Y. Hou, X. Yang, and Q. H. Abbasi, "Efficient AoA-based wireless indoor localization for hospital outpatients using mobile devices," *Sensors*, vol. 18, no. 11, pp. 3698–3715, 2018.

[25] N. Bnilam, D. Joosens, R. Berkvens, J. Steckel, and M. Weyn, "AoA-based localization system using a single IoT gateway: An application for smart pedestrian crossing," *IEEE Access*, vol. 9, pp. 13 532–13 541, 2021.

[26] Z. Yang, F. Wang, and W. Gong, "Mobi-Track: Distilling direct path in time domain for high accuracy WiFi tracking," in *Proc. IEEE Int. Conf. Pervasive Comput. Commun. Workshops (PerCom Workshops)*, 2021, pp. 287–292.

[27] X. Tong, H. Wang, X. Liu, and W. Qu, "MapFi: Autonomous mapping of Wi-Fi infrastructure for indoor localization," *IEEE Trans. Mobile Comput.*, p. 1, 2021.

[28] E. Soltanaghaei, A. Kalyanaraman, and K. Whitehouse, "Multipath triangulation: Decimeter-level WiFi localization and orientation with a single unaided receiver," in *Proc. 16th Annu. Int. Conf. Mobile Syst. Appl. Serv. (MobiSys)*, 2018, pp. 376–388.

[29] Z. Li, Z. Tian, and M. Zhou, "Decimeter level indoor localization using hybrid measurements of a distributed single receiver," *IEEE Trans. Instrum. Meas.*, vol. 70, pp. 1–14, 2021.

[30] X. Yang, J. Wang, W. Nie, and Y. Wang, "Passive localization of moving target with channel state information," *J. Sens.*, vol. 2021, pp. 1–9, 2021.

[31] K. Shamaei and Z. M. Kassas, "Receiver design and time of arrival estimation for opportunistic localization with 5G signals," *IEEE Trans. Wireless Commun.*, vol. 20, no. 7, pp. 4716–4731, 2021.

[32] X. Zhou, L. Chen, J. Yan, and R. Chen, "Accurate DoA estimation with adjacent angle power difference for indoor localization," *IEEE Access*, vol. 8, pp. 44 702–44 713, 2020.

[33] E. Y. Menta, N. Malm, R. Jantti, K. Ruttik, M. Costa, and K. Leppanen, "On the performance of AoA-based localization in 5G ultra-dense networks," *IEEE Access*, vol. 7, pp. 33 870–33 880, 2019.

[34] H. L. Van Trees, *Optimum Array Processing: Part IV of Detection, Estimation, and Modulation Theory*. New York: Wiley Interscience, 2004.

[35] B. Mamandipoor, D. Ramasamy, and U. Madhow, "Newtonized orthogonal matching pursuit: Frequency estimation over the continuum," *IEEE Trans. Signal Process.*, vol. 64, no. 19, pp. 5066–5081, 2016.

[36] Remcom, "Wireless insite - 3D wireless prediction software," 2021. [Online]. Available: https://www.remcom.com/wireless-insite-em-propagation-software